Quench in a pancake coil wound with REBCO Roebel cable: Model and validation

Quench in a Pancake Coil Wound with REBCO Roebel Cable: Model and Validation

Lorenzo Cavallucci[1], Marco Breschi[1], Pier Luigi Ribani[1], Qingbo Zhang[2], Yifeng Yang[2]

[1]Department of Electrical, Electronic, and Information Engineering, University of Bologna, 40136 Bologna, Italy
[2]Institute of Cryogenics, Faculty of Engineering and the Environment, University of Southampton, SO18 Southampton, United Kingdom

E-mail: lorenzo.cavallucci3@unibo.it

January 2021

Abstract. Roebel cables assembled with High Temperature Superconducting (HTS) tapes are a promising technology for several AC and DC applications. Their mechanical flexibility and compact design, combined with the capability of REBCO tapes to carry high transport currents in intense magnetic fields make them suitable for the application both in power devices and high field magnets. In this paper, an electro-thermal finite-element model (FEM) developed at the University of Bologna (Italy) is described. The model allows computing the current and heat redistribution between the strands of the cable and from turn to turn inside a winding through non-uniform distributed thermal and electrical resistances between strands. The tape is 'homogenized' so as to create an anisotropic continuum model through a previously developed homogenization technique. The model is validated by comparison with quench tests performed on a well instrumented 7-turn pancake coil wound with a 2-m long Roebel cable composed of 15 REBCO tapes. The experiments were performed at the University of Southampton (UK) in the frame of the R&D activities of the EuCARD-2 project. The quench decision time, the temperature and electric potential evolution, the current and heat redistribution between strands in the event of a quench are analysed and discussed in the present study.

Keywords: HTS, Quench, Roebel, Modelling. Submitted to: *Supercond. Sci. Technol.*

1. Introduction

The Roebel bar technique was proposed more than a century ago, in 1912, by Ludwig Roebel for copper cables to be used in generator technology [1]. This technique is based on the continuous transposition of flat strands along the cable length, which allows the current to better redistribute between them. In their superconducting version based on REBCO coated conductors, Roebel cables can carry high transport currents in DC conditions at high magnetic fields. Moreover, they exhibit low coupling losses in AC conditions given the reduction of magnetic flux linked to the loops

formed by the strands due to their transposition. The compactness of the conductor design and its mechanical flexibility makes it suitable for application in various fields, such as accelerator magnets [2] [3], fusion magnets [7], motors, generators and transformers [4] [6].

Both the computation of losses in electrodynamic transients and the analysis of stability and quench in Roebel-based devices is crucial for their safe operation. Several electromagnetic finite element or network models were recently developed to study Roebel cables in both DC and AC operating conditions. Two-dimensional models were proposed to study magnetization AC losses [8] and the current redistribution in the cable cross section [9]. In the analysis of electromagnetic transients, further progresses were the development of 3 D FEM models based on different approaches: the H-formulation was proposed in [10] [11] and the $\mathbf{T}$-Ω formulation in [12] [13].

The aforementioned models describe the electromagnetic transients in Roebel cables, but do not include the coupling with a thermal model for the stability and quench analysis. The quench studies for superconductor magnets are of paramount importance for their reliability and safe operation, as clearly demonstrated by the body of literature on the subject. Their relevance to Roebel cables is due to the additional complexity in the current sharing among the transposed strands. Current sharing is crucial to the quench behaviour of HTS conductors, which can benefit from a much wider temperature range for current sharing as compared to LTS. However, experimental quench studies on high current cables are very challenging. Given these premises, the development of sophisticated modeling tools is valuable, and validation is indispensable.

In [14], a 1 D thermal model with coupled turns is introduced to describe the heat propagation in Roebel-based magnets. A coupled electromagnetic and thermal network model for the time dependent modelling of magnetization and thermal runaways was proposed in [15] [16]. This model was based on a 3 D approach, applying the thin strip approximation to describe the tape geometry.

In [17] a different modeling approach was proposed for the electro-thermal modeling of REBCO Roebel cables, based on the discretization of the heat balance equation and of the current density continuity condition in a 1 D mesh, which determines a considerable reduction of the model unknowns still retaining the description of the main physical phenomena occurring during quench.

In the meanwhile, several experimental investigations of quench initiation and propagation in Roebel-based devices were performed at liquid helium temperature [18]. However, quench measurements at liquid nitrogen temperature have not extensively been performed and require further investigations, given the considerably different working conditions, in terms of material properties (specific heat, thermal and electrical conductivities of the materials) and temperature margin with respect to the current sharing temperature. To this purpose, a dedicated experiment was performed at the University of Southampton with a heavily instrumented Roebel cable [19] [20].

In the present work, the experimental activity is expanded to enable quench measurements close to adiabatic conditions with variable external disturbances in a pancake coil wound with Roebel cable. This type of measurement is extremely difficult for high current Roebel cables. A true adiabatic condition with cooling at the current injection only is not experimentally viable due to the long length ($\sim > 1$ m) required for a representative current sharing at multiples of the transposition pitch (~ 0.25 m). On the other hand, a cable quench study becomes unrepresentative and impossible with a cable cooled in a cryogenic fluid. In this work, quench measurements are performed

as much as possible close to adiabatic condition due to the negligible heat exchange with the cooling bath on the top and bottom surfaces of the coil. The coil is epoxy impregnated and an epoxy layer (0.5 mm-1.0 mm) left between the liquid nitrogen pool boiling and the strands thus acting as a thermal insulation layer. The contact area between the impregnation layer and the strands on the top of the coil is about 40-times lower than the lateral area of the strands.

Figure 1: Roebel-based coil under investigation at the University of Southampton [20].

This work also proposes an electro-thermal model of coils wound with Roebel cables developed at the University of Bologna, which accounts for heat and current redistribution between strands of the cable and for heat redistribution between the turns of the coil. Given the remarkable complexity of the analysed system, several numerical techniques are put in place to reduce the computational burden. The coil model main bricks are the detailed tape and Roebel cable models developed in [21] and [17] respectively. The Roebel cable model proposed in [17] is extended here to pass from the description of the cable itself to that of a Roebel-based pancake coil. The additional features of the model include the description of heat transfer to the liquid nitrogen bath, the distributions of magnetic flux density and field angle relative to the tape over the whole pancake coil, the epoxy impregnation, and the thermal contact between coil turns at the strand level. The numerical method is validated here by comparison to experimental results, thus pointing out the reliability of the model to precisely reproduce not only the local voltage-tap signals and hot-spot temperatures of strands, but also the global quench energies of the coil.

The first part of this paper describes the details of the model, based on the definition of a homogenized anisotropic material of the strand, thermal and electrical contact resistances between strands/coil turns and reduced dimensionality. The second part of the paper describes in detail the experimental results obtained in the setup of the University of Southampton, and the validation of the proposed model by comparison with the measurements. A detailed analysis of the voltage signals along the coil is reported, and adopted to retrieve important information concerning the current redistribution length and time constants, the longitudinal and radial heat propagation, the quench propagation velocity and the minimum quench energy.

2. The REBCO Roebel Coil: Model Description

In this work, the equations of the stationary electrodynamics coupled with the heat transfer equation with a source term inside the coil are solved using a FE method.

In the actual implementation, the straightened cable axis is discretized along its whole length by means of a 1 D mesh based on linear elements. A set of the thermal and electrical equations is written for an array of variables and solved on this mesh. The unknowns of the array are the temperatures and electric potentials of all N-strands of the cable, plus the temperature of the insulation layer. A sketch of the model unknowns on each node of the 1 D mesh is shown in Figure 2 and a list of the main functions and variables is reported in Table 1.

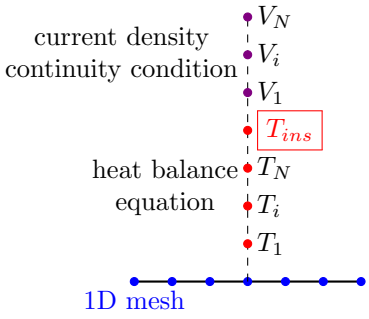

Figure 2: Sketch of the model structure of a N-strands Roebel cable.

2.1. Electrical Model

The electrical model of the Roebel coil is based on a set of equations solved for an array of variables representing the electric potentials $[V_1, \ldots, V_{N_t}]$ of all strands computed with respect to a reference value located on one terminal of the cable, where the electric potential is set to zero.

The current density continuity condition can be written for the i-th strand as ($i = 1 \ldots N_t$):

$$\nabla \cdot \mathbf{J}_i = 0 \tag{1}$$

Since $\mathbf{J}_i = -\sigma_i \nabla V_i$, the equation (1) can be simplified accounting for the contributions along the longitudinal (ξ) and across the transverse (y) directions (see Figure 3).

In the 1 D discretization, the term corresponding to the y direction can be discretized as

$$\frac{\partial J_{y,i}}{\partial y} = \sum_j f_{i,j}(\xi)\ \sigma_{\mathrm{el}}^{\mathrm{c}}\ \frac{V_j(\xi,t) - V_i(\xi,t)}{\delta} \tag{2}$$

The equation (2) describes the current redistribution between the strands in contact via the distributed electrical contact conductance $\sigma_{\mathrm{el}}^{\mathrm{c}}$ in $\mathrm{S\,m^{-2}}$ between the two strands and δ is the thickness of the strand. The function $f_{i,j}(\xi)$ describes the local contact area between the i-th and the j-th strand; its values are included between 0 and 1. The function is equal to 1 at the regions of overlapping between the two strands, while it is null where the two strands are not in contact. Equation (1) is then simplified as:

$$\frac{\partial}{\partial \xi}\left(-\sigma_i\,(T_i, E_i)\,\frac{\partial V_i(\xi,t)}{\partial \xi}\right) = \sum_j f_{i,j}(\xi)\ \sigma_{\mathrm{el}}^{\mathrm{c}}\ \frac{V_j(\xi,t) - V_i(\xi,t)}{\delta} \tag{3}$$

Table 1: List of Main Variables and Functions of the FEM Model

	Electrical Model	
E_i	V/m	electric field of i-th strand
V_i	V	electric potential of i-th strand
$\sigma_{\mathrm{el}}^{\mathrm{c}}$	$\mathrm{S\,m^{-2}}$	electrical contact conductance between adjacent strands
σ_i	$\mathrm{S\,m^{-1}}$	homogenized longitudinal electrical conductivity
I_{op}	A	coil operating current
	Thermal Model	
T_i	K	temperature of i-th strand
T_0	K	nitrogen pool boiling temperature
T_{ins}	K	temperature of turn-to-turn insulation layer
$T_{\mathrm{s},i}$	K	temperature of insulation top surface
ρ	$\mathrm{kg\,m^{-3}}$	homogenized density
c_{p}	$\mathrm{J/(kg\,K)}$	homogenized specific heat
k	$\mathrm{W\,m^{-1}\,K^{-1}}$	longitudinal thermal conductivity
k_{ins}	$\mathrm{W\,m^{-1}\,K^{-1}}$	thermal conductivity of insulation
h	$\mathrm{W\,m^{-1}\,K^{-1}}$	heat transfer coefficient towards liquid nitrogen
$R_{\mathrm{th}}^{\mathrm{c}}$	$\mathrm{K\,m^2\,W^{-1}}$	thermal contact resistance between adjacent strands
$R_{\mathrm{th,ins}}^{\mathrm{c}}$	$\mathrm{K\,m^2\,W^{-1}}$	thermal contact resistance between i-th strand and insulation
$Q_{i,j}^{\mathrm{J}}$	$\mathrm{W\,m^{-3}}$	Joule power due to current between adjacent strands
$Q_{i,j}^{\mathrm{c}}$	$\mathrm{W\,m^{-3}}$	heat conduction between adjacent strands
Q_i^{in}	$\mathrm{W\,m^{-3}}$	heat conduction between strands and insulation at the inner
Q_i^{out}	$\mathrm{W\,m^{-3}}$	heat conduction between strands and insulation at the outer
$Q_i^{\mathrm{LN}}(\xi,t)$	$\mathrm{W\,m^{-3}}$	heat transfer towards liquid nitrogen
$Q_i^{\mathrm{h}}(\xi,t)$	$\mathrm{W\,m^{-3}}$	heater thermal disturbance
	Geometrical Variables and Functions	
ξ	m	longitudinal coordinate
w	m	strand width
δ	m	strand thickness
δ_{ins}	m	thickness of insulation
S_{tot}	m	total cross section of strand
$f_{i,j}$	-	contact function between i-th and j-th strands
f_i^{in}	-	contact function between i-th strand and insulation at inner turn
f_i^{out}	-	contact function between i-th strand and insulation at outer turn

where $\sigma_i\left(T_i(\xi,t), E_i(\xi,t)\right)$ is the homogenized longitudinal electrical conductivity in $\mathrm{S\,m^{-1}}$ as a function of temperature and electric field E_i ($E_i(\xi,t) = -\partial V_i(\xi,t)/\partial\xi$).

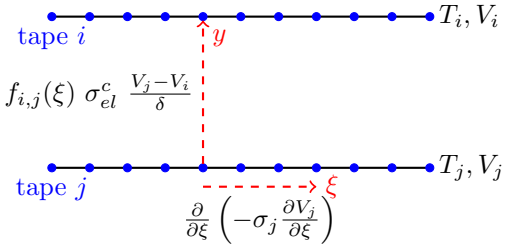

Figure 3: Sketch of the electrical model.

As boundary condition, on both terminals of the coil, an equipotential surface is

imposed for all strands. On the inner terminal, the current density J_i^{in} is imposed for the i-th strand ($i = 1, \ldots, N_{\text{t}}$) as:

$$J_i^{\text{in}} = \sum_{\substack{j=1 \\ j \neq i}}^{N_{\text{t}}} \sigma_j \left(T_j, E_j\right) \frac{\partial V_j}{\partial \xi} + \frac{I_{\text{op}}\left(t\right)}{S_{\text{tot}}} \tag{4}$$

where I_{op} is the time dependent operating current and S_{tot} the total cross section of the strand.

2.2. Thermal Model

As already mentioned, only one strand is discretized and a set of heat transfer equations is solved for an array of thermal elements $[T_1, \ldots, T_{N_{\text{t}}}, T_{\text{ins}}]$ describing the temperatures of all the N_{t} strands of the cable plus the turn-to-turn insulation layer (T_{ins}).

The thermal equation can be written for the i-th temperature element $T_i(\xi, t)$ as:

$$\rho\, c_{\text{p}}(T_i)\, \frac{\partial T_i(\xi,t)}{\partial t} - \frac{\partial}{\partial \xi}\left(k(T_i)\, \frac{\partial T_i(\xi,t)}{\partial \xi}\right) = \sigma_i\left(T_i, E_i\right)\left(\frac{\partial V_i(\xi,t)}{\partial \xi}\right)^2 + \sum_j^{N_{\text{t}}} Q_{i,j}^{\text{J}}(\xi,t) +$$

$$+ \sum_j^{N_{\text{t}}} Q_{i,j}^{\text{c}}(\xi,t) + Q_i^{\text{h}}(\xi,t) + Q_i^{\text{out}}(\xi,t) + Q_i^{\text{in}}(\xi,t) - Q_i^{\text{LN}}(\xi,t) \tag{5}$$

where $T_i(\xi)$ is the temperature of the i-th element as a function of the longitudinal direction ξ, ρ the homogenized density in $\mathrm{kg\,m^{-1}}$, $c_{\text{p}}(T_i)$ the temperature dependent homogenized specific heat in $\mathrm{J\,kg^{-1}\,K^{-1}}$, and $k(T_i)$ the temperature dependent longitudinal thermal conductivity in $\mathrm{W\,m^{-1}\,K^{-1}}$.

In the heat transfer equation, the first term on the right hand side is the longitudinal ohmic heating due to current flow along the strands. The term $Q_{i,j}^{\text{J}}$ represents the Joule power due to the current exchange between the i-th and j-th strand in contact:

$$Q_{i,j}^{\text{J}}\left(\xi\right) = \sum_j \frac{1}{2}\, f_{i,j}(\xi)\, \sigma_{\text{el}}^{\text{c}}\, \frac{\left(V_i(\xi,t) - V_j(\xi,t)\right)^2}{\delta} \tag{6}$$

The function $f_{i,j}(\xi)$ is the same as that in (2) for current transfer between adjacent strand through electric contacts. The term $Q_{i,j}^{\text{J}}$ is computed assuming that the Joule power due to current exchange between two strands is equally split between them.

The heat conduction $Q_{i,j}^{\text{c}}$ by contact between adjacent strands, also modulated by $f_{i,j}(\xi)$, is modelled as:

$$Q_{i,j}^{\text{c}}\left(\xi\right) = \sum_j f_{i,j}(\xi) \frac{T_i(\xi,t) - T_j(\xi,t)}{R_{\text{th}}^{\text{c}}\ \delta} \tag{7}$$

where R_{th}^{c} in $\mathrm{K\,m^2\,W^{-1}}$ is the distributed thermal contact resistance between the two strands and δ the thickness of the strand.

The thermal contact between turns is described through the heat flux $Q_i^{\text{out}}(\xi,t)$ and $Q_i^{\text{in}}(\xi,t)$ towards the insulation located at the inner part of the turn and at the

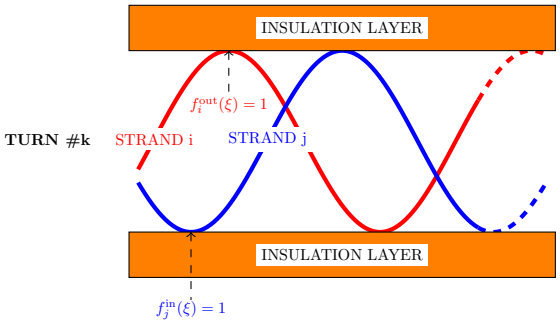

Figure 4: Sketch of the functions $f_i^{\text{out}}(\xi)$ and $f_i^{\text{in}}(\xi)$.

outer one respectively. For the i-th strand, the heat exchange with the insulation layer is computed as:

$$Q_i^{\text{out}}(\xi,t) + Q_i^{\text{in}}(\xi,t) = f_i^{\text{out}}(\xi)\,\frac{T_i(\xi,t) - T_{\text{ins}}(\xi',t)}{R^{\text{c}}_{\text{th,ins}}(T_{\text{ins}})\;\delta} + f_i^{\text{in}}(\xi)\,\frac{T_i(\xi,t) - T_{\text{ins}}(\xi',t)}{R^{\text{c}}_{\text{th,ins}}(T_{\text{ins}})\;\delta} \tag{8}$$

where ξ and ξ' are the longitudinal coordinate corresponding to the contact between the i-th strand and the insulation layer respectively. The functions $f_i^{\text{out}}(\xi)$ and $f_i^{\text{in}}(\xi)$, shown in Figure 4, describe the contact between the considered strand and the insulation at the outer and at the inner turns respectively:

$$f_i^{\text{out}}(\xi) = \begin{cases} 1 & \text{contact with the insulation} \\ 0 & \text{no contact with the insulation} \end{cases} \tag{9}$$

The thermal contact resistance $R^{\text{c}}_{\text{th,ins}}$ between strands and insulation layer is computed by considering the thickness δ_{ins} and the thermal conductivity k_{ins} of the fiberglass layer acting as an inter-turn insulation.

$$R^{\text{c}}_{\text{th,ins}} = \frac{\delta_{\text{ins}}}{k_{\text{ins}}(T_{\text{ins}}(\xi',t))} \tag{10}$$

The thermal disturbance introduced by a heater located at half length of strand #7 is modelled by the term $Q_i^{\text{h}}(\xi,t)$.

As boundary condition, adiabatic conditions are assumed for the coil. On the last turn, all strands are assumed in contact through a contact resistance with the external copper ring at 77 K. On the inner terminal of each strand, the temperature is set to 77 K. The same temperature is imposed as initial condition over the whole cable length.

2.3. Liquid Nitrogen Bath

The heat transfer towards the pool boiling liquid nitrogen is expressed by the term $Q_i^{\text{LN}}(\xi,t)$:

$$Q_i^{\text{LN}}(\xi,t) = \frac{h\,(T_{\text{s},i}(\xi,t) - T_0)\,(T_{\text{s},i}(\xi,t) - T_0)}{w} \tag{11}$$

where w is the tape width, h is the heat transfer coefficient, T_0 is the nitrogen pool boiling temperature, set to 77 K. $T_{\mathrm{s},i}(\xi,t)$ is the temperature on the surface of the insulation layer on the top of the coil, directly in contact on one side with the i-strand and on the other side with the pool of liquid nitrogen.

The temperature $T_{\mathrm{s},i}$ is computed solving the non linear heat balance on the impregnation layer:

$$h\left(T_{\mathrm{s},i}(\xi,t)-T_0\right)\left(T_{\mathrm{s},i}(\xi,t)-T_0\right) = k_{\mathrm{ins},s}\left(T_{\mathrm{s},i}(\xi,t)\right)\frac{T_i(\xi,t)-T_{\mathrm{s},i}(\xi,t)}{\delta_{\mathrm{ins},s}} \tag{12}$$

where $k_{\mathrm{ins},s}$ and $\delta_{\mathrm{ins},s}$ are respectively the thermal conductivity and the thickness of the insulation layer on the top of the coil.

The nucleate and film boiling conditions are modeled by different formulations of the cooling coefficient h. In particular, the following relations, presented in [22] and [23], are implemented:

$$h(\Delta T) = a + b\,\Delta T^4 \qquad (\Delta T = 2-11\,\mathrm{K}) \qquad \text{(nucleate boiling)} \tag{13}$$

$$h(\Delta T) = \frac{c+d\,\Delta T}{1+e\,\Delta T} \qquad (\Delta T = 20-200\,\mathrm{K}) \qquad \text{(film boiling)} \tag{14}$$

where the coefficients a, b, c and d are reported in [23]. The boiling regimes for a liquid nitrogen bath as computed through the relations reported above are shown in Figure 5.

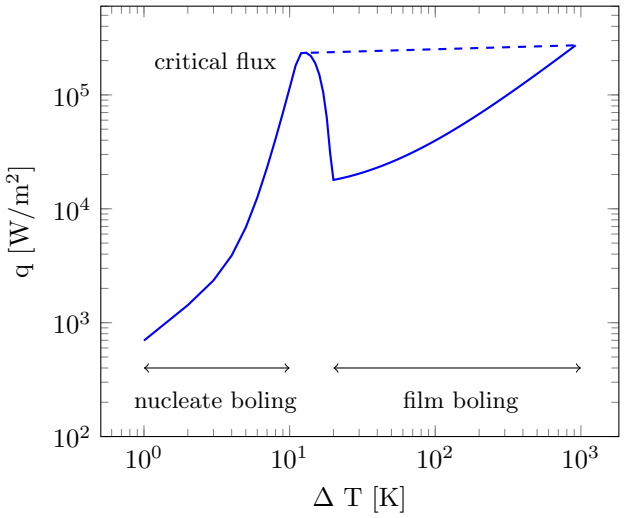

Figure 5: Liquid nitrogen boiling regimes.

2.4. Magnetic Flux Density Calculation

The computation of the magnetic flux density generated by the coil is computed through a 3D semi-analytical and numerical approach [24]. The code [24] computes the magnetic flux density on the cross section of the Roebel cable by taking into

account the exact coil geometry. The self-field components $B_x(x, y, \xi)$ and $B_y(x, y, \xi)$ are computed as a function of the coil current on the cross section of the cable (x-y plane) along the azimuthal direction (ξ):

$$B_x(x, y, \xi, t) = b_x(x, y, \xi)\, I_{\mathrm{op}}(t) \tag{15}$$
$$B_y(x, y, \xi, t) = b_y(x, y, \xi)\, I_{\mathrm{op}}(t) \tag{16}$$

The coefficients $b_r(x, y, \xi)$ and $b_z(x, y, \xi)$ are computed by applying a constant unit current flowing in the coil, and then used during the time dependent simulations.

The strand critical current exhibits a strong dependence on the field angle θ between the magnetic flux density vector and the c-axis of the strand [25][26]. The strand orientation with respect to the magnetic field has to be taken into account by computing the field angle θ at every location.

2.5. Homogenization Procedure

In order to avoid the discretization of each strand into its constituent layers, a homogenization procedure is applied to calculate the thermal and electrical conductivities. The electrical conductivity σ_i of the i-th strand is computed assuming all the N_l layers of the strand as in parallel connection [27]. The homogenized electrical conductivity is estimated as:

$$\sigma_i = \frac{I_{\mathrm{c}}(T_i, B_i, \theta_i)}{E_{\mathrm{c}}\ S_{\mathrm{tot}}} \left(\frac{1}{E_{\mathrm{c}}} \frac{\partial V_i(\xi, t)}{\partial \xi} \right)^{\frac{1-n}{n}} + \sum_{j=1}^{N_l} \sigma_j^{\mathrm{nc}}(T_i, B_i)\ \frac{S_j}{S_{tot}^{\mathrm{nc}}} \tag{17}$$

where $I_{\mathrm{c}}(T_i, B_i, \theta_i)$ is the critical current as a function of temperature, magnetic flux density and field angle, E_{c} is the critical electric field set to $10^{-4}\,\mathrm{V\,m^{-1}}$, n the n-value of the power law set to 20, σ_j^{nc} and S_j^{nc} respectively the electrical conductivity and the cross section of the normal conducting j-th layer of the i-th strand.

A similar procedure is adopted for the computation of the longitudinal thermal conductivity k_i of the i-th strand.

The dependence of the critical current on the magnetic field, temperature and field angle is described by the parameterization reported in [25], [28] and [29]. The critical current is computed according to the following expression:

$$I_{\mathrm{c}}\,(T, B, \theta) = I_{\mathrm{c0}}\, \frac{1}{1 + \dfrac{B}{B_0}} \left(\mathrm{w} \cos^2(\theta) + \sin^2(\theta) \right)^{-0.5} \exp\left(-\frac{(T - T_0)^k}{T^*} \right) \tag{18}$$

3. Configuration of the REBCO Roebel Coil

The model was configured to represent the REBCO Roebel coil used in the experimental study [19] [20] for comparison and validation.

Superconducting strands and Roebel cable. A piece of 2 m-long Roebel cable of 15 strands of REBCO tapes (Bruker EST) was wound into a pancake coil. The critical current of the tape in the coil self field was about 33 A. The cable, with a

Table 2: Main Parameters of the Bruker Tape.

Tape Geometrical Parameters		
thickness	copper	50 µm
	YBCO	1 µm
	buffer layer	0.2 µm
	stainless steel	100 µm
width		5.8 mm
copper RRR		30
Tape Critical Current Parameters		
Ic_0		57.2
B_0		0.11
w		0.82
T_0		77 K
T^*		12.5 K
k		2.0
n-value		20

Table 3: Main Parameters of the REBCO Roebel Cable and of the Pancake Coil.

Roebel Cable	
transposition pitch T_p	226 mm
transposition angle T_θ	50°
cable width	12 mm
strands number	15
Pancake Coil	
turns number	7
inner radius	72 mm
inter-strand insulation layer δ_{ins}	200 µm
top pancake insulation layer $\delta_{\text{ins},s}$	500 µm

transposition pitch of 226 mm, was assembled at KIT (Germany). Table 2 lists the main geometrical dimensions of the REBCO tape and the parameters of the critical current parametrization determined by fitting the critical current measurements presented in [19] [20]. The main geometric parameters of the Roebel cable are given in Table 3. These parameters were used for assigning the values of function $f_{i,j}(\xi)$ in (2), (6), and (7).

Pancake coil. The Roebel cable was wound into a pancake coil of 7 turns with 72 mm inner diameter. The coil former consisted of a inner G10 cylinder inserted inside a copper ring for current injection. The outer surface of the copper ring was precisely machined into a single turn spiral with the pitch equal to the cable thickness. The outer surface of the copper ring was precisely machined into a single turn spiral in the direction of the winding with the pitch equal to the cable thickness. After the first turn was wound on and soldered to the copper ring, it was continued smoothly to the second turn, starting exactly on top of the start of the first turn. Neither the strands nor the cable are insulated, nonetheless all the turns were co-wound with a 200 µm-thick fiberglass ribbon working as inter-turn electrical insulation layer. On the

4-th turn of the coil, a miniature heater was attached on strand #7 at the inner face of the turn (between turns #4 and #3). The last turn was soldered on top of the outer copper, which is machined into a spiral and inserted between the last two turns so that the soldering is on the superconductor side of the strands as in the inner contact. A stainless-steel shim was wound around the last turn of the Roebel cable prior to soldering it to the outer copper ring and remained as the outer enforcement. In the end, the coil was impregnated with epoxy insulation (StycastTM) that penetrate between turns and also work as inter-turn electrical insulation layer [30]. The 200 µm-thick fiberglass prevents delamination due to mismatch of the thermal expansion coefficient between the epoxy and the REBCO strands.

The main geometric parameters of the pancake coil implemented in the model are given in Table 3.

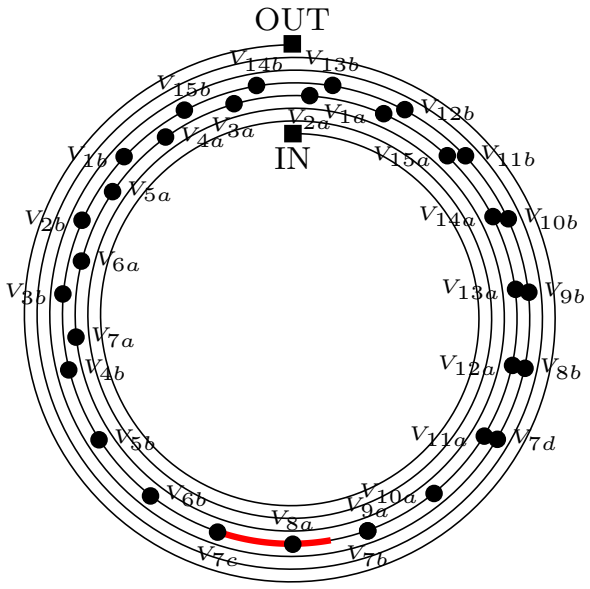

Figure 6: Sketch of the REBCO coil and detail of the voltage taps position.

Heaters and sensors. The heater was a miniature resistor chip attached to a copper shim which was soldered to the exposed transition section of strand #7 at the 4-th turn. A pair of voltage taps V_{ia} and V_{ib} ($i = 1, \ldots, 15$) was soldered to each strand at its exposed transition section either side of the heater as shown in Figure 6. The intent was to set voltage taps on all strands each side of the heater to monitor the quench propagation during the tests. The voltage taps were separated by exactly the length of a transposition pitch except for strand #7, where V_{7a} and V_{7b} were two pitch lengths apart and two additional taps, V_{7c} and V_{7d}, were soldered next to either side of the heater. The "a" and "b" taps were closer to the inside and outside current

Table 4: Electrical and Thermal Contacts between Adjacent Strands

	reference set-up	modified set-up
$\sigma_{\mathrm{el}}^{\mathrm{c}}$	$2.0 \times 10^7\,\mathrm{S/m^2}$	$3.0 \times 10^7\,\mathrm{S/m^2}$
$R_{\mathrm{th}}^{\mathrm{c}}$	$7.0 \times 10^{-4}\,\mathrm{K\,m^2/W}$	$3.5 \times 10^{-4}\,\mathrm{K\,m^2/W}$
	$7.0 \times 10^{-3}\,\mathrm{K\,m^2/W}$ (heater zone)	$3.5 \times 10^{-3}\,\mathrm{K\,m^2/W}$ (heater zone)

contacts respectively. The voltage differences V_i were recorded during measurements:

$$\Delta V_i = V_{ia} - V_{ib} \qquad \forall i = 1, \ldots, 15 \tag{19}$$

$$\Delta V_{7-0} = V_{7a} - V_{7c} \tag{20}$$

The inductive component of the voltages was minimised by counter-winding V_{ib} to V_{ia} along the cable to form 15 twisted pairs. A thermocouple was soldered in the middle of the copper shim to measure the hot spot temperature.

Material properties. The homogenised thermo-electrical properties of the REBCO tape were also largely defined by its consituent metalic components, dominated by copper stabiliser and stainless substrate (Table 2). The superconducting properties were found by measurements on short samples of conductor strands [19] [20] and fitted to (18) with the relevant parameters given also in Table 2. The epoxy impregnated fibre-glass insulation was assumed to have thermal properties similar to those of G10, i.e. $c_{p,\mathrm{ins}}(T) \approx c_{p,\mathrm{G10}}(T)$ and $k_{\mathrm{ins}}(T) \approx k_{\mathrm{G10}}(T)$.

Quench measurements. The quench was studied in liquid nitrogen pool with a transport current up to 400 A, more than 90 % of the critical current of the coil. To induce a quench experimentally, heating pulses at different power levels and durations were fired via the heater while the voltages and temperatures along the coil were recorded simultaneously.

4. Results and Validation

Although most of the material properties for the Roebel pancake coil cannot be changed significantly when comparing the model with the experimental studies, the thermal contact resistance $R_{\mathrm{th}}^{\mathrm{c}}$ and electrical contact conductances $\sigma_{\mathrm{el}}^{\mathrm{c}}$ between adjacent strands are two remaining parameters that can be adjusted for validating the model by finding a match to the experimental results.

4.1. Quench Case at 8.8 J *Heater Pulse: Hot Spot Temperature*

Figure 7 shows the quench of the coil at a transport current of 400 A, obtained by depositing 8.8 J on the heater with a 1.0 W heater pulse (right axis) of 8.8 s. The blue trace shows the corresponding hot spot temperature recorded experimentally, rising sharply upon the onset of the heater pulse at $t = 0$ s to 95 K, above T_c, within ∼1 s. Then, the temperature increases slowly to 98 K during the heater pulse and rapidly decreases after the end of the heater pulse at $t = 8.8$ s. The temperature drop slows down towards ∼79.5 K, and finally rises again at $t \sim 11.5$ s due to an irreversible

quench, as shown in the inset in Figure 7. At about $t = 13.25\,\mathrm{s}$, the quench protection system intervened by cutting the transport current and the temperature consequently decreased.

The solid red line in Figure 7 shows the hot spot temperature, here referred as T_7, upon the $1\,\mathrm{W}/8.8\,\mathrm{s}$ heater pulse by modelling with the reference $\sigma_{\mathrm{el}}^{\mathrm{c}}$ and $R_{\mathrm{th}}^{\mathrm{c}}$ given in Table 4. It was also necessary to increase the thermal contact resistance (Table 4) by an order of magnitude at the heater region to account for the presence of the copper shim and the soldering material between the strand #7 and the neighbouring ones.

The tentative approach towards irreversible quench at 8.8 J pulse suggested the deposited energy was fairy closed to the minimum quench energy (MQE) for 400 A. The model indeed found recovery for a heater energy of 8.4 J heater pulse as shown by the dashed red line in Figure 7. In this case, after the heater pulse, the temperature decreased at a faster rate towards 77 K. The slight temperature increase observed in the quench case after the heater pulse, shown in the inset in Figure 7, is not here observed due to the negligible impact of the joule heating.

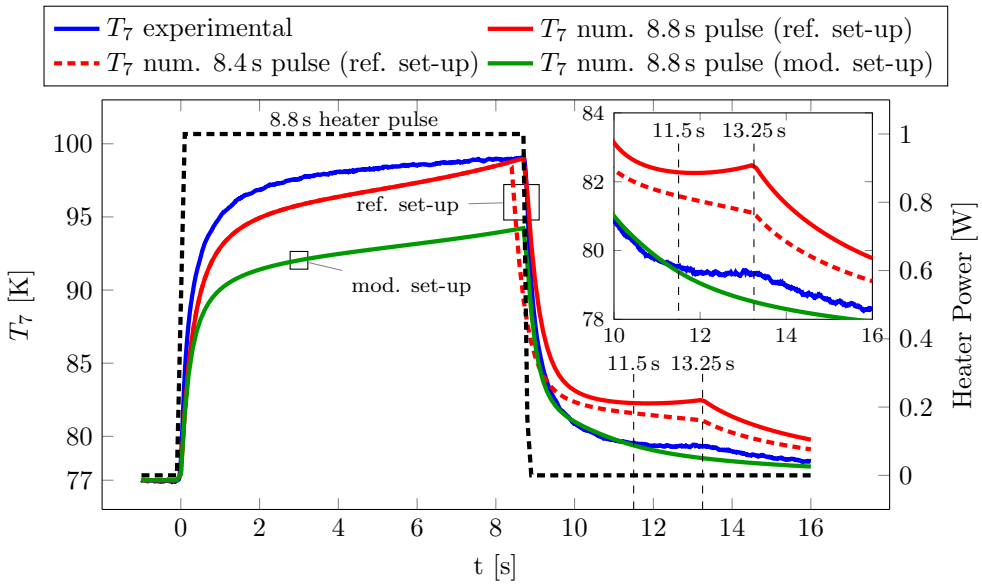

Figure 7: Temperature evolution in strand #7. The experimental quench test is compared on the left axis with the numerical results in case of quench and recovery with the reference and modified inter-strand parameters. An inset between t = 10 s - 16 s is added. On the right axis, the heater pulse profile.

The model founds the recovery of the coil with a 50 % higher electrical contact conductance, i.e. $\sigma_{\mathrm{el}}^{\mathrm{c}} = 3.0 \times 10^{7}\,\mathrm{S\,m^{-2}}$, together with a 50 % lower thermal contact resistance, i.e. $R_{\mathrm{th}}^{\mathrm{c}} = 3.5 \times 10^{-4}\,\mathrm{K\,m^{2}\,W^{-1}}$, as shown by the solid green line in Figure 7. During the pulse, the temperature found with the modified set-up is about 6 K lower than the experimental temperature. Most important, this temperature clearly shows a recovery: the temperature does not exhibit the temperature increase observed at $t \sim 11.5\,\mathrm{s}$ in the quench case. The temperature computed with the reference set-up (solid red line) exhibits the temperature increase at $t \sim 11.5\,\mathrm{s}$, even if

this temperature is higher than the experimental one (solid blue line). These results confirm the validity of the reference thermal and electrical contact parameters reported in Table 4.

It is worth noting that the experimental temperature shown in Figure 7 is recorded by a thermocouple soldered to the copper shim where also the heater is attached. Hence, the temperature sensor is not directly located on the strand. The copper shim and the soldering material are not modelled in detail, therefore some discrepancies during quench between the numerical and experimental results are expected.

4.2. Quench Energy and Stability: Impact of Heater Power

The impact of heater power on quench energy is investigated with an operating temperature of 77 K and transport current set to 400 A. In Figure 8, the quench energies measured during tests are compared with the numerical results obtained with the reference inter-strand electrical conductance and thermal resistance reported in Table 4. This set-up of parameters is able to correctly reproduce the experimental results.

The impact of the contact parameters is investigated by computing the quench energies with the modified set-up reported in Table 4.

For heater powers above 0.8 W, the contact conductances have negligible impact on quench energies. The quench energy is stable about 9 J. The impact is remarkable for power values below 0.8 W. In this case, the quench energies computed with modified contact conductances exhibits an increase even above 60 %. The higher is the contact conductances, the better is the heat flux and current redistribution between strands and the more stable is the coil in case of quench event.

If the heater power is below 0.4 W, even long heater pulses are not able to quench the coil. The heat flux and currents redistribute between strands without transition to the normal state. In case of higher contact conductances, no quench occurs also for power between 0.4 W and 0.46 W. The stability of the coil is increased by 15 %.

4.3. Quench Case at 8.8 J *Heater Pulse: Temperature and Heat Flux Redistribution*

Further to showing agreement with the experimental results on quench energy and hot spot temperature, the model is able to describe the evolution of the normal zone profile and the radial diffusion across the inter-strand and inter-turn contacts.

In case of transport current of 400 A and heater pulse of 1 W/8.8 s, the computed values of temperatures of the strands at the end of the heater pulse at t = 8.8 s is shown in Figure 9. Figure 9 clearly indicates a heat propagation between the strands of the same turn and from turn to turn. An insight of the temperature profiles of turn #3 and #4 is shown respectively in Figures 9(b) and 9(c) along the longitudinal cable coordinate from 0.45 m - 0.75 m and 0.75 m - 0.95 m respectively. These results allow to compare the effects of the turn-to-turn heat flux distribution with respect to the strand-to-strand heat propagation.

The heater is located on strand #7 at turn #4 directly in contact with the insulation layer between turns #3 and #4. On turn #4, the temperature of the strands #6 and #8, adjacent to strand #7, rise up immediately due the heat transfer from strand #7 within the turn redwhile the temperature of strands far from the strand #7, as #1 and #15, does not increase significantly during the heater pulse.

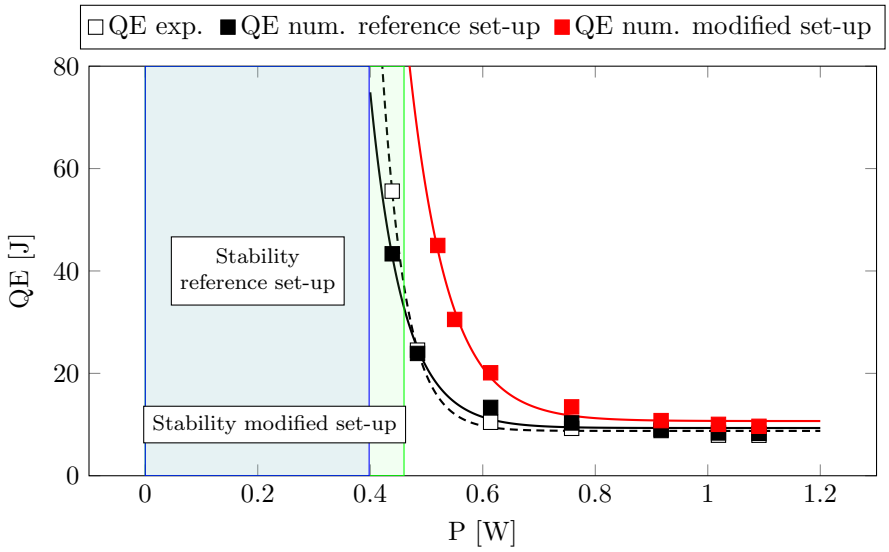

Figure 8: Impact of heater power on quench energies. The experimental results are compared with the energies computed with two different set-up of contact conductances.

On turn #3, the turn-to-turn heat flux across the insulation layer increases the temperature of the strands which are in direct contact with it, such as strands #1 and #15. This temperature enhancement is in some cases even greater than that found on the strands of turn #4. As a matter of fact, strands #1 and #15 exhibits higher temperatures at turn #3 than at turn #4, even if turn #3 is not directly heated. This shows that the turn-to-turn heat propagation in this experiment is relevant and comparable to the one between the strands in the cable at the same turn.

No significant temperature increase are visible on the strands of turn #5, which is also adjacent to turn #4, but on the opposite side of the heater (located between turns #4 and #3). In this case, the time delay of the heat propagation across the whole cable thickness is longer than the heater pulse.

The overall heat fluxes at the heater location, given by summing up the contributions of all strands in the cable in the longitudinal and radial directions, are shown in Figure 10. The three main flux components are depicted: $q_{r_{43}}$ and $q_{r_{45}}$ are the radial heat fluxes between turns #4-#3 and #4-#5 respectively, q_{L_4} is the heat flux in the longitudinal direction along turn #4. The heat pulse per-unit-surface entering strand #7 from the heater, q_{heater}, is also reported in the figure.

It is worth noting that the overall heat power in the longitudinal direction q_{L4} is greater than that in radial direction $q_{r_{43}}$ and $q_{r_{45}}$. The aforementioned difference between the temperature rises of the strands in turns #3 and #5 is also confirmed by comparing the significant value of $q_{r_{43}}$ to that of $q_{r_{45}}$ which is practically negligible.

4.4. Quench Case at 8.8 J *Heater Pulse: Voltage Profile and Current Redistribution*

The voltage signals measured over the various strands show the typical rise during the thermal runaway. The comparison between experimental and numerical results is shown in Figure 11. A good agreement is found between numerical and experimental

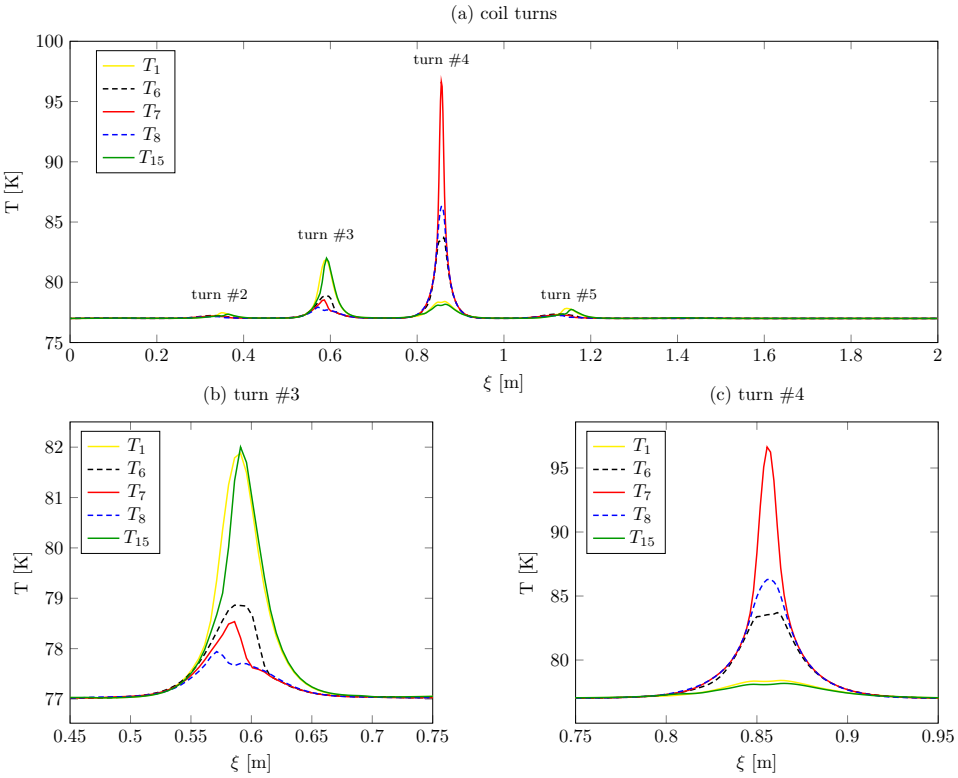

Figure 9: Strands temperature distribution at t = 8.8 s on (a) all coil turns, (b) turn #3 and (c) turn #4.

values.

The peak voltage, which is important for the design of the quench protection system, is below 5 mV for all measurements except $\Delta V_6, \Delta V_9, \Delta V_{10}$ which exhibit a peak voltage between 5 mV and 6 mV.

The signals ΔV_6, ΔV_{7-0}, ΔV_8 and ΔV_9 clearly indicate the development of the normal zone, which is particularly evident in ΔV_{7-0}. In the time interval between 2 s and 8 s, the heater pulse determines an initial voltage rise. Between 9 s and 11 s, the voltage development initially slows down for the effects of cooling and then accelerates again due to the normal zone formation and propagation. Above 11 s, the joule heat is dominant and the voltage rises up irreversibly until the transport current switch off at 13.25 s.

Figure 12 shows the time evolution of the current for the strands #1, #4, #6, #7, #8, #10, #12, #15 at the heater location. As the heater is immediately fired at 0 s, the current on strand #7, directly in contact with the heater, decreases. The strands #6 and #8, in close contact with #7, also exhibit a current drop due to the temperature increase. The current is therefore redistributed towards the neighbouring strands #1, #4, #10, #12, #15. At 13.25 s, the currents of the strands decrease to zero due to the switch-off of the transport current in the experiment.

As shown in Figure 12, if the transport current is maintained constant during quench, the current redistribute for about 20 s - 25 s after the heater pulse. On the

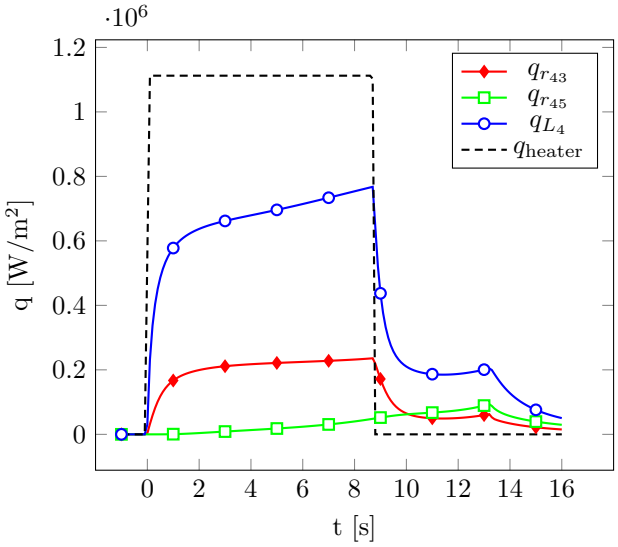

Figure 10: Heat flux on the heater in the longitudinal and radial direction.

right axes of Figure 12, the terminal voltage of the coil is shown. The voltage starts from about 10^{-4} V and reaches about 1 V after 40 s if the quench protection system lacks of intervene.

To study the current transfer, we report in the following the transverse current densities between strands. The current density $J_{h,k}$ is taken positive if the current flows from strand h to strand k.

In Figure 13, the value of the transverse current density flowing between strands #7-#6 is shown along the cable length at t = 1.0 s, corresponding to the minimum of current on strand #7 as shown in Figure 12.

It is worth noting that the current flow between these strands exhibits a periodic pattern; this is related to the contact area between the strands and is modelled by the function f_{76} shown on the right y-axes. Given the peculiar network of contacts in this region, the transverse current density J_{76} is null where there is no direct contact between the two strands. The redistribution length is of course affected by the pattern of contacts between the strands. The transverse current density between strands #6 and #7 is in the range $[-0\,5 + 1.5\,\mathrm{kA\,m^{-2}}]$. The corresponding current redistribution region extends over the cable length in a region of about 0.8 m before the miniature heater located between 0.85 m and 0.86 m. After the heater, the current redistribution is practically negligible.

The transverse current densities between strands #5-#6, #7-#8 and #8-#9 at t = 1.0 s are also added in Figure 14. Similar redistribution length are found for these strands. This result confirms the current is exiting the strand #7 towards the neighbouring ones, i.e. #6 and #8.

The voltage measured at the terminal of the coil is shown in Figure 15. The experimental result is compared with the numerical one (in case of stainless steel substrate) confirming the reliability of the model to reproduce the global electrical behaviour of the coil.

The materials assembling REBCO tapes are a crucial point in the technology

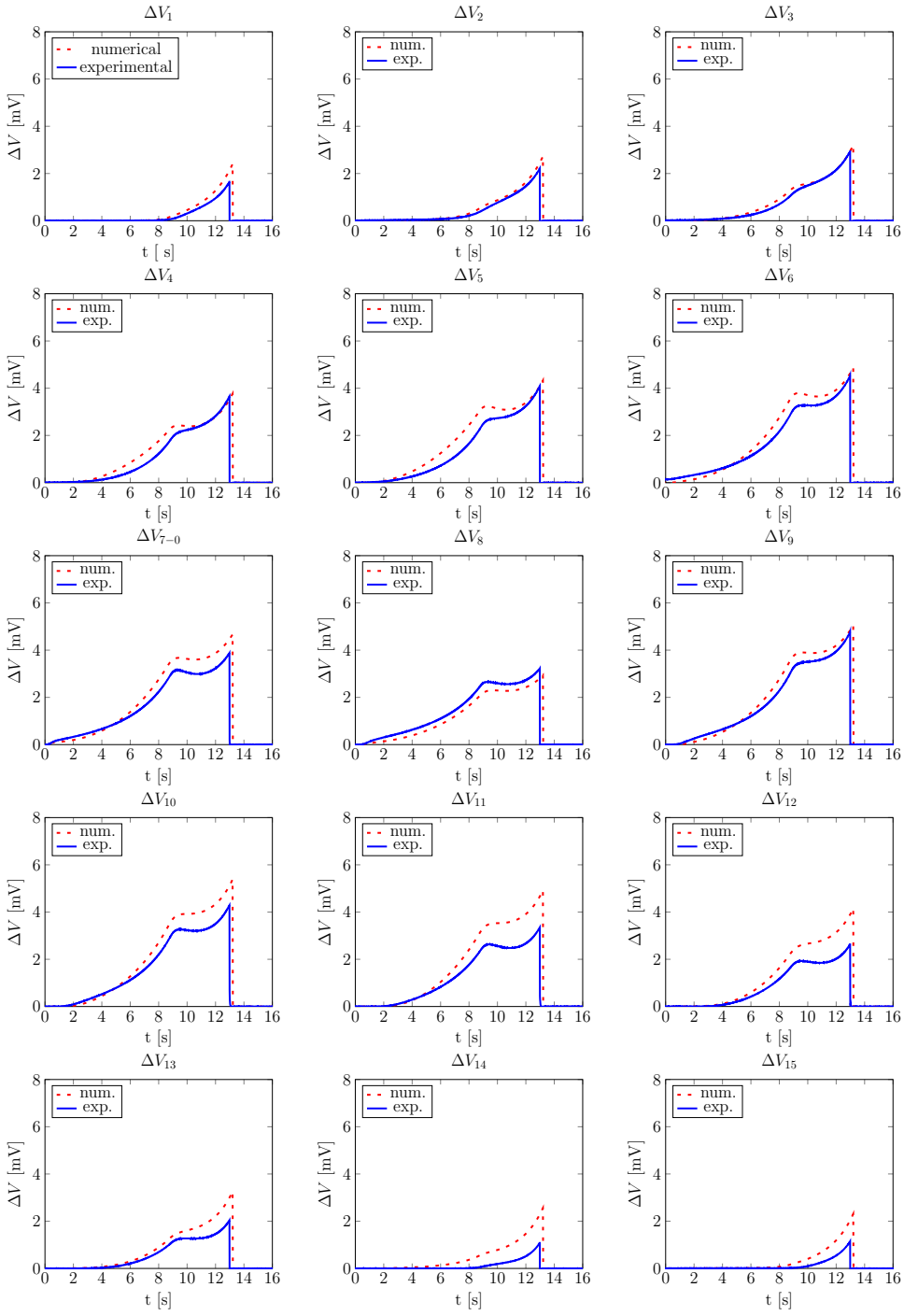

Figure 11: Numerical and experimental voltage measurements.

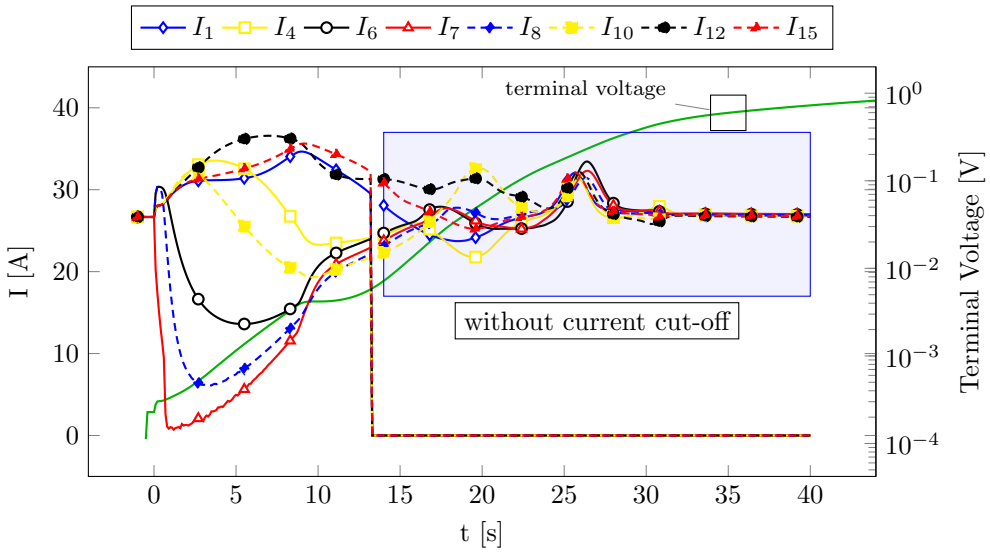

Figure 12: Current redistribution for strands #1, #4, #6, #7, #8, #10, #12, #15 at the heater location with and without current cut-off. On the right axes, the terminal voltage of the coil without current cut-off.

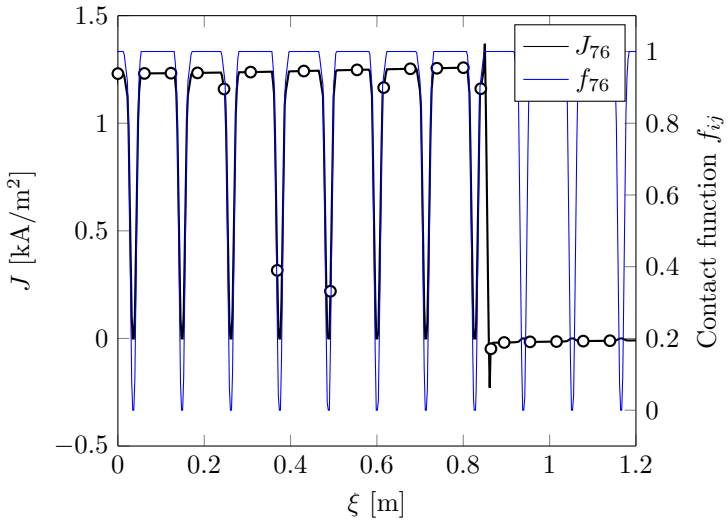

Figure 13: Transverse current density distribution along the coil at t = 1.0 s between strands #7-#6 J_{76} (left y-axes) versus the contact function f_{76} (right y-axes).

of HTS magnets. As a matter of fact, most companies assemble their tapes with different material working as a substrate such as Hastelloy, nickel-tungsten alloy or stainless steel. This last material is, in fact, the one used in the present work. In Figure 15, the terminal coil voltages obtained with the experiment and with the

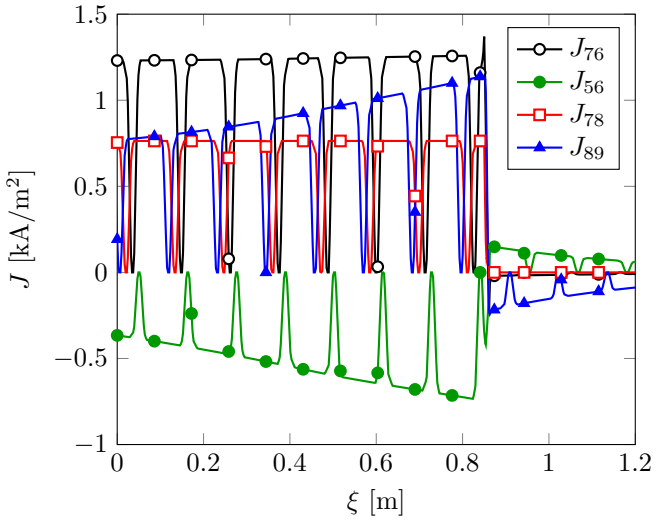

Figure 14: Transverse current density distribution along the coil at t = 1.0 s between strands #7-#6, #5-#6, #7-#8 and #8-#9.

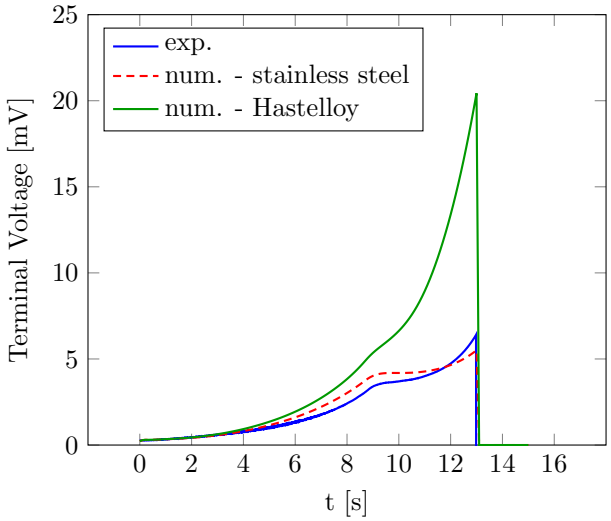

Figure 15: Terminal voltage of the Roebel Coil. The experimental result is compared with two numerical tests. In the first test, the substrate of REBCO tapes is supposed stainless steel while, in the second case, it is Hastelloy.

numerical computation in case of stainless steel substrate are compared with the numerical result in case of Hastelloy. In this last case, the terminal voltage is four time higher than the voltage with stainless steel because of the lower electrical conductivity of Hastelloy with respect of stainless steel. This result is important for a proper design of the quench protection system and of the threshold voltage to prevent damage during the tests.

4.5. Longitudinal Normal Zone Propagation Velocity

The analysis of normal zone propagation velocity (NZPV) in the longitudinal direction is based on the temperature distribution of the strands along the coil length. As example, the temperatures of strands #7 and #15 are shown in Figure 16.

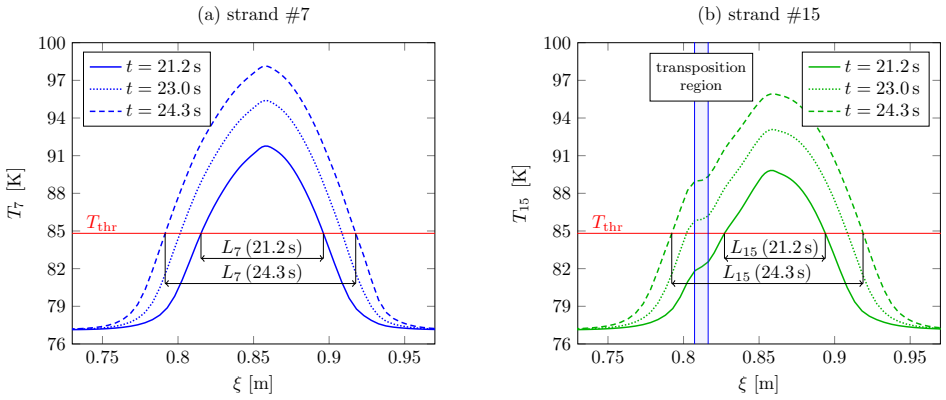

Figure 16: Strands temperature distribution at t = 21.2 s, t = 23 s and t = 24.3 s of (a) strand #7 and (b) strand #15.

The time window $t_1 = 21.2\,\mathrm{s}$ - $t_2 = 24.3\,\mathrm{s}$ is selected as a reference. At $t = 21.2\,\mathrm{s}$, all strands exhibit a temperature exceeding the threshold temperature T_{thr} while before t_1 the temperature of some strands is below T_{thr}. The threshold temperature T_{thr} is here defined as the average value of the critical temperature T_{c}, equal to 91 K, to the current sharing temperature T_{cs}, equal to 78.6 K. At $t = 24.3\,\mathrm{s}$, the temperatures of all strands are above the critical temperature T_{c}, after t_2 some strands exhibit temperatures below T_{c}. Only in the time window 21.2 s - 24.3 s, all strands exhibit a temperature above the threshold temperature T_{thr}.

The time window $t_1 = 21.2\,\mathrm{s}$ - $t_2 = 24.3\,\mathrm{s}$ defines the length of the normal zone front for the i-th strand, respectively $L_i\,(t_1)$ and $L_i\,(t_2)$. The normal zone front is detailed in Figure 16.

The normal zone propagation velocity is consequently computed for the i-th strand as:

$$\mathrm{NZPV}_i = \frac{1}{2}\frac{L_i\,(t_2) - L_i\,(t_1)}{t_2 - t_1} \qquad i = 1,\ \ldots,\ 15 \tag{21}$$

In Figure 17, the NZPV computed in the time window 21.2 s - 24.3 s is shown for all strands. Strands #2 to #8 and #10 to #14 exhibit velocities between 0.7 and $0.8\,\mathrm{cm\,s^{-1}}$. The NZPV of strand #9 is below $0.7\,\mathrm{cm\,s^{-1}}$ while strands #1, #11 and #15 exhibit velocities higher than $0.8\,\mathrm{cm\,s^{-1}}$.

In particular, strand #15 exhibits normal zone velocity up to about $1\,\mathrm{cm\,s^{-1}}$. The temperature profile of this strand is characterized by a local temperature decrease between 0.90 m and 0.91 m, detailed in Figure 16 (b). This region correspond to the transposition of the strand and the loss of contact with the neighbouring strands. As a matter of fact, the temperature plateau corresponding to the transposition region increases the normal zone front and consequently the propagation velocity.

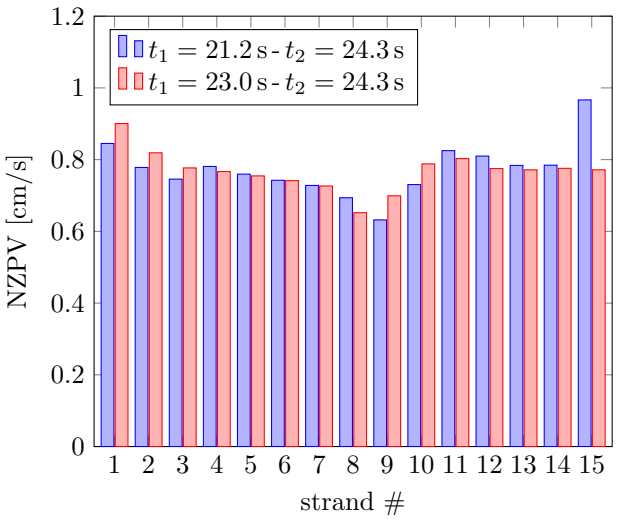

Figure 17: Normal zone propagation velocities of the strands. The results based on the time window 21.2 s - 24.3 s are compared with the velocities computed with the window 23.0 s - 24.3 s.

In Figure 16, the temperatures of strands #7 and #15 at $t = 23\,\mathrm{s}$ are added. At $t = 23\,\mathrm{s}$, the temperature of strands #7 and #15 are between the profiles at $t = 21.2\,\mathrm{s}$ and at $t = 24.3\,\mathrm{s}$. At $t = 23\,\mathrm{s}$, the temperature plateau of strand #15 is above the threshold temperature and it does not affect the NZPV. In Figure 17, the NZPV computed in the time window 23 s - 24.3 s is shown. The NZPV is estimated in this further time window to remark the impact of the transposition pitch on the propagation velocity. Strand #15 exhibits a velocity below $0.8\,\mathrm{cm\,s^{-1}}$ instead of $1\,\mathrm{cm\,s^{-1}}$. In this case, strand #15 does not exhibit a velocity higher than other strands, as previously found in the time window 21.2 s - 24.3 s.

Strands #1 and #15, far from the strand directly heated, are more affected by the selection of the time window. The transposition region has an higher impact on the propagation front of these strands and consequently on the normal zone velocity.

It is worth of noting that after 24 s, the length of the normal front is about 126 mm, no longer than half of the twist pitch of the cable, equal to 113 mm. The propagation of the normal zone in the cable is slowed further because of the spare capacity in the strands during the heat pulse even at transport current corresponding to 90 % of the critical current. This slow propagation velocity has impact on the design of the quench protection system: a fast intervention is essential to prevent damage to the coil. As shown in Figure 12, if the quench protection system does not intervene, after 24 s, the terminal voltage of the coil is above 0.1 V at an overall dissipation of 40 W mostly confined in a normal zone no more than 126 mm long and propagating slowly at less than $1\,\mathrm{cm\,s^{-1}}$. The found values are within the range of the results in literature [32], [33].

5. Conclusion

This work presents a comprehensive numerical and experimental investigation of quench in a Roebel-based pancake coil. The experimental set-up realized enables

one to measure voltage signals and hot-spot temperatures during quench close to adiabatic conditions, which is extremely difficult for high current Roebel cables. The high reliability of the coil shown in this study is hard to attain, especially considering the challenges to the fabrication of 2 G-based coils, and shows the robustness of the coil construction procedure developed. As a matter of fact, the coil has undergone many thermal cycles from ambient to different temperatures as low as 4.2 K and has been subjected to more than 100 quenches with current up to 1700 A without showing any degradation of the performance. The measurements presented here show the impact of the power of the external disturbance on the quench energy of a Roebel-based HTS coil.

The results gained during the experimental campaign were investigated with an electro-thermal model for the analysis of quench in Roebel-based magnets.

The main tasks involved in the modelling of HTS Roebel coils are related to the high aspect ratio of the HTS tapes, the complex geometry of the coil, and the coupled thermal and electromagnetic problem. In this study, these challenges are solved by different techniques. A homogenized material is adopted to tackle the problem of the high aspect ratio of the REBCO conductor. A reduced dimensionality approach enables handling the complex coil geometry and the coupling of the electromagnetic and thermal processes. In this approach, the heat transfer equation and the current density continuity condition are solved over a 1 D mesh for an array of temperatures and voltages of the strands and the insulation layer. The contact between strands belonging to the same turn or different turns is described through thermal and electrical contact resistances.

The close agreement between experimental and numerical results - in terms of voltage signals, hot-spot temperature and quench energies - shows the reliability of the model to reproduce not only the local propagation of the normal zone front but also the global quench energies of the coil. The adjustable parameters of the model are successfully narrowed down to only two, i.e. the thermal and electrical contact resistances among the Roebel strands, that are important practical informations for cable and coil manufacturers. These results show that the model retains the key functional characteristics of the cable without a full 3D description of the coil geometry, which is essential for the volume of parametric studies carried out here. More importantly, simplicity allows a better interrogation and understanding of the model.

The temperature profiles of the strands are presented to compare the contribution of longitudinal and radial (turn-to-turn) heat distribution during quench. The heat flux in the longitudinal direction is the main contribution nonetheless the flux from turn-to-turn is not negligible. The heater location affects the radial heat flux. Since the heater is attached between turns #3 and #4, the radial flux between turns #4 and #5 is negligible with respect to that between turns #3 and #4.

The quench energies computed with the reference contact resistances at different heater power values are able to reproduce the experimental results. In this case, the coil is stable for heater power values below 0.4 W. The heat flux and currents redistribute between strands and no quench occurs. The contact resistances between strands have a remarkable impact on quench energies: if the contact resistances are decreased of 50 %, the coil is stable also for heater power values between 0.4 Wand 0.46 W, corresponding to an increase of 15 %.

The current sharing between strands is depicted: if one of the strands quenches, the current redistributes between the neighbouring ones thus increasing the stability

of the cable. The current transfer length can reach the whole cable length, and the redistribution phenomenon may take up to 25 s.

The normal zone propagation velocity in the longitudinal direction is computed here based on the temperature threshold corresponding to the average value between the critical temperature and the current sharing temperature. The results show a spread of velocities between strands in the range $0.6\,\mathrm{cm\,s^{-1}}$ - $1\,\mathrm{cm\,s^{-1}}$, corresponding to a variation of about 40 %. The transposition region of the strands affects the propagation of the normal zone front with a consequent increase of the propagation velocity. Further investigations are required to analyse the impact of the Roebel cable geometry on the propagation of the normal zone front not only in the longitudinal direction but also in the radial direction, i.e. between coil turns.

In conclusion, the proposed experimental procedure and the developed modeling approach are suitable for a precise description of the main phenomena occurring during quench in a Roebel-based coil. The key phenomena identified and quantified are the current sharing among transposed strands, the heat flux redistribution between coil turns and the propagation of the normal zone front. The results point out not only the impact of the power level of external disturbances on the coil quench energy, but also the effect of thermal and electrical inter-strand contact resistance on the stability of the Roebel-based coil.

References

[1] German Patent: Ludwig Roebel (BBC company) 19th March 1912.

[2] Rossi L *et. al.* 2015 The EuCARD-2 Future Magnets European Collaboration for Accelerator-Quality HTS Magnets *IEEE Trans. Appl. Supercond.* **25** 4001007-4001007

[3] Kirby G A *et. al.* 2015 Accelerator-Quality HTS Dipole Magnet Demonstrator Designs for the EuCARD-2 5-T 40-mm Clear Aperture Magnet *IEEE Trans. Appl. Supercond.* **25** 4000805-4000805

[4] Leghissa M *et. al.* H-W 2006 kA-class high-current HTS conductors and windings for large scale applications *presented at the 5th Int. Conf. on Science and Engineering of Novel Superconductors* CIMTEC 2006, Acireale, Italy

[5] Song P *et. al.* 2018 Design and test of a double pancake coil for SMES application wound by HTS Roebel cable *IEEE Trans. Appl. Supercond.* **28** 5701205

[6] Glasson N *et. al.* 2011 Development of a 1 MVA 3-Phase Superconducting Transformer Using YBCO Roebel Cable *IEEE Trans. Appl. Supercond.* **21** 1393-1396

[7] Goldacker1 W *et. al.* 2009 Status of high transport current ROEBEL assembled coated conductor cables *Supercond. Sci. Technol.* **22** 034003

[8] Otten S *et. al.* 2020 Anisotropic monoblock model for computing AC loss in partially coupled Roebel cables *Supercond. Sci. Technol.* **33** 094013

[9] Vojenciak M*et. al.* 2011 Effect of self-field on the current distribution in Roebel-assembled coated conductor cables *Supercond. Sci. Technol.* **24** 09500

[10] Zermeno V *et. al.* 2013 A full 3D time-dependent electromagnetic model for Roebel cables *Supercond. Sci. Technol.* **26** 052001

[11] Grilli F *et. al.* 2013 AC Losses of Pancake Coils Made of Roebel Cable *IEEE Trans. Appl. Supercond.* **23** 5900205

[12] Nii M *et. al.* 2012 Corrigendum: Three-dimensional model for numerical electromagnetic field analyses of coated superconductors and its application to Roebel cables *Supercond. Sci. Technol.* **25** 095011

[13] Amemiya N *et. al.* 2014 Alternating current loss characteristics of a Roebel cable consisting of coated conductors and a three-dimensional structure *Supercond. Sci. Technol.* **27** 035007

[14] Ruuskanen J *et. al.* 2017 Predicting Heat Propagation in Roebel-Cable-Based Accelerator Magnet Prototype: One-Dimensional Approach With Coupled Turns *IEEE Trans. Appl. Supercond.* **27** 0600205

[15] Van Nugteren J 2016 High Temperature Superconducting Accelerator Magnets *Ph.D. thesis, University of Twente* Available: https://cds.cern.ch/record/2228249/files/CERN-THESIS-2016-142.pdf

[16] Van Nugteren J *et. al.* 2015 Study of a 5 T Research Dipole Insert-Magnet Using an Anisotropic ReBCO Roebel Cable *IEEE Trans. Appl. Supercond.* **24** 4000705
[17] Cavallucci L *et. al.* 2018 Electrothermal Modeling of Quench in REBCO Roebel Cables *IEEE Trans. Appl. Supercond.* **28** 4703405
[18] Kirby G A *et. al.* 2017 First Cold Powering Test of REBCO Roebel Wound Coil for the EuCARD2 Future Magnet Development Project *IEEE Trans. Appl. Supercond.* **27** 4003307
[19] Zhang Q *et. al.* 2018 Performance and Quench Characteristics of a Pancake Coil Wound with 2G YBCO Roebel Cable *IEEE Trans. Appl. Supercond.* **28** 4801005
[20] Zhang Q *et. al.* 2019 Quench Characteristics of a Roebel Cable Pancake Coil at 77 K *presented at the 14th European Conference on Applied Superconductivity* EUCAS 2019, Glasgow, UK
[21] Casali M *et. al.* 2015 Two-Dimensional Anisotropic Model of YBCO Coated Conductors *IEEE Trans. Appl. Supercond.* **25** 6600112
[22] Kida L M *et. al.* 1981 Pool-Boiling Heat Transfer in Liquid Nitrogen *J. Nucl. Sci. Technology* **28** 501-513
[23] Sumption M *et. al.* 2017 Stability, quench and current sharing in Roebel and CORC cables for HEP magnets *presented at the 13th European Conference on Applied Superconductivity* EUCAS 2017, Geneva, Swiss
[24] Fabbri M *et. al.* 2001 A Priori Error Bounds on Potentials, Fields, and Energies Evaluated With a Modified Kernel *IEEE Trans. Magn.* **37** 2970-2976
[25] Hilton D K *et. al.* 2015 Practical fit functions for transport critical current versus magnitude and angle data from (RE)BCO coated conductors at fixed low temperature and in high magnetic fields *Supercond. Sci. Technol.* **28** 074002
[26] Breschi M *et. al.* 2017 Modeling of Quench in the Coupled HTS Insert/LTS Outsert Magnet System of the NHMFL *IEEE Trans. Appl. Supercond.* **27** 4301013
[27] Breschi M *et. al.* 2016 Analysis of quench in the NHMFL REBCO prototype coils for the 32 T magnet project *Supercond. Sci. Technol.* **29** 055002
[28] Rostila L *et. al.* 2007 How to determine critical current density in YBCO tapes from voltagecurrent measurements at low magnetic fields *Supercond. Sci. Technol.* **20** 1097
[29] Senatore C *et. al.* 2016 Field and temperature scaling of the critical current density in commercial REBCO coated conductors *Supercond. Sci. Technol.* **29** 014002
[30] Bailey W *et. al.* 2011 Testing of a lightweight coreless HTS synchronous generator cooled by subcooled liquid nitrogen, *IEEE Trans. Appl. Supercond.* **21** 11591162
[31] Otten S *et al.* 2017 Inter-strand resistance in REBCO Roebel cables and effect on AC loss *presented at the 13th European Conference on Applied Superconductivity* EUCAS 2017, Geneva, Swiss
[32] Pelegrn J *et. al.* 2011 Numerical and Experimental Analysis of Normal Zone Propagation on 2G HTS Wires *IEEE Trans. Appl. Supercond.* **21** 3041
[33] Van Nugteren J *et. al.* 2015 Measurement and analysis of normal zone propagation in a ReBCO coated conductor at temperatures below 50 K *Physics Procedia* **67** 945951